






## Quantum light transport in phase-separated Anderson localization fiber

Alexander Demuth <sup>1✉</sup>, Robin Camphausen <sup>1</sup>, Álvaro Cuevas <sup>1✉</sup>, Nick F. Borrelli<sup>2</sup>, Thomas P. Seward III<sup>2</sup>, Lisa Lamberson<sup>2</sup>, Karl W. Koch<sup>2</sup>, Alessandro Ruggeri <sup>3</sup>, Francesca Madonini<sup>4</sup>, Federica Villa<sup>4</sup> & Valerio Pruneri <sup>1,5✉</sup>

Propagation of light by Anderson localization has been demonstrated in micro-nano-structured fibers. In this work, we introduce a phase separated glass Anderson localization optical fiber for quantum applications. By using a spontaneous parametric down-conversion source, multi-photon detection with a single-photon avalanche diode array camera, and signal post-processing techniques, we demonstrate quantum light transport, where spatial correlations between photon pairs are preserved after propagation. In order to better understand and improve light transport, we study light localization, observing a dependence on wavelength. Our results indicate that the proposed phase separated fiber may become an effective platform for quantum imaging and communication.

<sup>1</sup>ICFO-Institut de Ciències Fotòniques, The Barcelona Institute of Science and Technology, 08860 Castelldefels, Barcelona, Spain. <sup>2</sup>Science and Technology Division, Corning Incorporated, Corning, NY 14831, USA. <sup>3</sup>Micro Photon Devices SRL, Via Waltraud Gebert Deeg 3f, 39100 Bolzano, Italy. <sup>4</sup>Dipartimento di Elettronica, Informazione e Bioingegneria-Politecnico di Milano, Piazza Leonardo da Vinci 32, 20133 Milano, Italy. <sup>5</sup>ICREA-Institució Catalana de Recerca i Estudis Avançats, Passeig Lluís Companys 23, 08010 Barcelona, Spain. ✉email: [alexander.demuth@icfo.eu](mailto:alexander.demuth@icfo.eu); [alvaro.cuevas@icfo.eu](mailto:alvaro.cuevas@icfo.eu); [valerio.pruneri@icfo.eu](mailto:valerio.pruneri@icfo.eu)

Anderson localization is defined as the absence of wave diffusion (e.g., light) caused by disorder in a medium<sup>1</sup>. 2D transverse Anderson localization of light (TAL) was predicted independently by Abdullaev and Abdullaev and by De Raedt et al.<sup>2,3</sup> and first demonstrated by Schwartz et al.<sup>4</sup>. The TAL effect can be harnessed to confine light beams in two dimensions during propagation along a third dimension, namely the longitudinal axis. This is realized by means of the TALOF (TAL optical fiber), a novel laterally disordered waveguide.

Besides being of interest to fundamental science, research on TALOFs has been substantially driven by their potential use in imaging and communication applications<sup>5</sup>. In particular, Karbasi et al.<sup>6</sup> showed that TALOF enables light transport through many parallel optical channels, which can be more densely distributed in space than possible with conventional multi-core fibers. This property is extremely interesting in the field of quantum communication and quantum imaging, where the faithful transmission of high-dimensional quantum states defined by their spatial correlations enables such diverse applications as quantum key distribution<sup>7</sup>, quantum ghost imaging, and low-light imaging in the presence of strong noise<sup>8,9</sup>. While the transmission of quantum states encoded in spatial modes is also possible with multi-mode fiber, in general this requires time-consuming characterization of the fiber transfer matrix as well as active wavefront control of the input light<sup>10</sup>. In contrast, TALOF is a passive transmission medium that requires neither active spatial light modulation nor precise alignment, and shows resilience to bending<sup>11</sup>.

Therefore, these advantages strongly suggest the use of TALOF in quantum communication and quantum imaging applications. However, while many experiments have already proven TALOF's ability to transmit classical light patterns<sup>5</sup>, a corresponding demonstration for quantum correlated light states has never been performed. Moreover, the eventual adoption of TALOF in real world use cases hinges upon the availability of an industrially scalable fabrication process. To date, using predominantly the stack-and-draw technique, first polymer–polymer<sup>12</sup>, then glass–glass<sup>13–15</sup>, and air–glass TALOFs<sup>11,16,17</sup> have been manufactured. More recently, femtosecond laser-writing has also been employed<sup>18</sup>, but all of the above fabrication methods are labor-intensive and cannot be scaled to an industrial process.

Here, we show the accurate transmission of spatial quantum correlations through a TALOF. We obtain this result using a novel TALOF based on phase-separated glass developed at Corning Inc.<sup>19–21</sup>, which we call phase-separated fiber (PSF) and which is fabricated in a scalable process. We therefore demonstrate critical ingredients needed for the use of TALOF in quantum-enabled applications.

The findings from this work demonstrate that high-dimensional quantum information can be transmitted through PSF, paving the way to practical quantum imaging and quantum communication with phase-separated Anderson localization fibers.

## Results

Our article is divided into three main sections. First, we introduce the PSF and describe the light transport mechanism. Second, we explore quantum light transport, where an overview of the experimental concept is depicted in Fig. 1. On the transmitter side, multi-photon quantum states of light are injected into the PSF. Those states are received on the other end, where quantum correlations are maintained during transmission. In our experiment, we use spontaneous parametric down-conversion (SPDC) to generate anti-correlated photon pairs in a massive spatial mode space. As seen in Fig. 1, after propagating through the PSF, we use a single-photon avalanche diode (SPAD) array detector to image photon coincidences at the output, confirming that non-classical correlations are maintained. In the third section, in order to optimize quantum light transport, we analyze the PSF's waveguiding properties. Our experiments reveal that localization and resolution are wavelength dependent, which we confirm with numerical finite-element simulations. Based on these results we discuss pathways to optimize PSF fabrication for improved future quantum applications.

**Waveguiding mechanism.** A PSF consists of many glass strands embedded in a glass matrix of different refractive index. It is fabricated in a drawing process, where borosilicate glass is heated up to close to the melting point, causing it to separate into two phases of different refractive index. The glass is then drawn into a cane or fiber, where the particulate phase forms elongated strands. The randomly varying position and size of these strands, and the refractive index difference between the phases, create lateral disorder.

In Fig. 2a we show a contrast image of a PSF sample fabricated in the same way as that used for light propagation experiments. Two phases in the cross-section—matrix glass with low refractive index (in white) and the strand inclusions with high refractive index (in black)—can be distinguished. By analyzing the image, we determined an average strand diameter  $d \sim 280$  nm (details in Methods). Fully vectorial eigenmodes of Maxwell's equations were computed by preconditioned conjugate-gradient minimization of the block Rayleigh quotient in a plane-wave basis, using a freely available software package<sup>22</sup>. In the simulation, we assumed

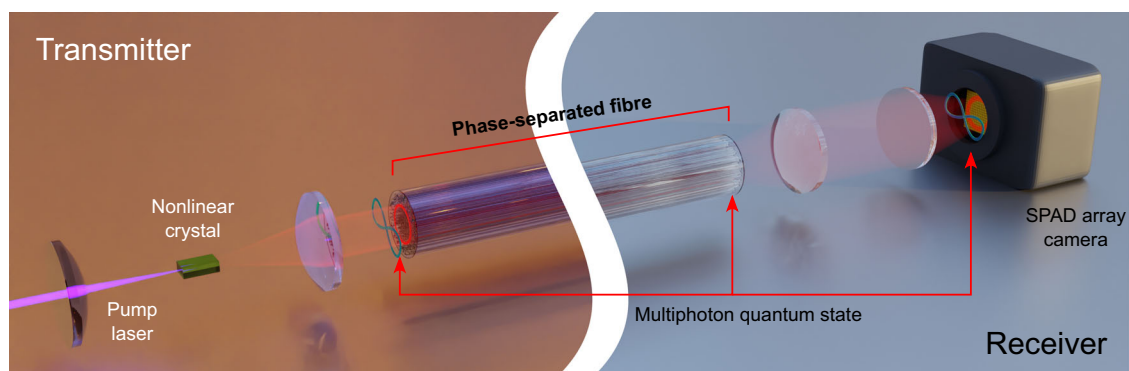


**Fig. 1 Schematic overview of the experiment.** We are able to transport and retrieve multiphoton states with quantum correlations with a phase-separated Anderson localization fiber; for that, we do not require a specific match between the ring-shape quantum light beam and the localized modes supported by the phase-separated Anderson localization fiber. We achieve this by performing photon coincidence imaging with a single photon avalanche diode (SPAD) array camera. This result suggests that phase-separated Anderson localization fiber could enable applications in quantum imaging or quantum communication.

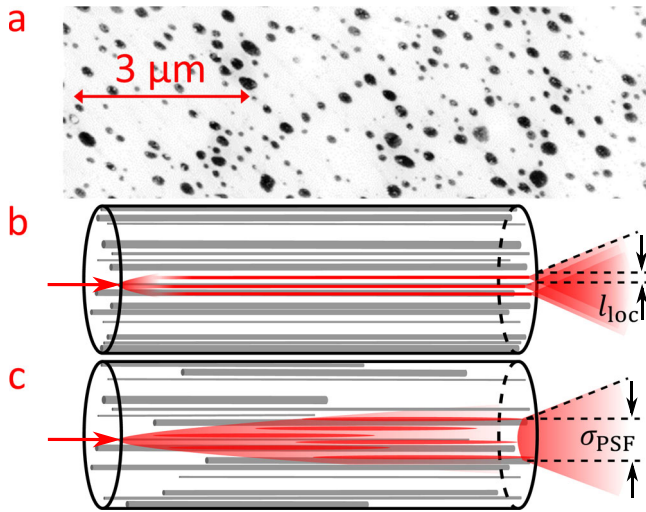


**Fig. 2 Phase-separated fiber: contrast image and schematic propagation through Anderson localized modes.** **a** Contrast image of a cross-section of a phase-separated fiber (PSF) sample, with matrix glass (in white) and strands (in black). The distribution of particle diameters is roughly Poissonian. The disorder in refractive index leads to the formation of localized modes. **b** Schematic of light propagation in an ideal PSF cane, where the axially invariant modes (red horizontal lines, with localization length  $l_{loc}$ ) are the main guiding channels. **c** Propagation in real PSF, where light is partially diffused, hopping between localized modes, which change adiabatically due to longitudinal discontinuities (here exaggerated). The output of the PSF then reaches a size  $\sigma_{PSF}$ .

that PSF is axially invariant, that means its cross-section remains the same throughout the whole length. Under these conditions, the PSF supports exponentially localized modes, originating from the lateral disorder (see Supplementary Information, Supplementary Fig. S1 in Supplementary Note 1: Localized modes examples, resulting from numerical simulation).

Schematically, light propagation in a perfect PSF is sketched in Fig. 2b. Initially, a beam rapidly expands, while the light beam intensity profile begins to match with transverse localized modes (red pattern)<sup>3</sup>. These modes serve as high-fidelity channels due to their low coupling. Their finite lateral size is characterized by the localization length  $l_{loc}$ , which constitutes the lower bound for the optical resolution of a TALOF.

In our experiment, we used non-ideal PSF samples, as illustrated in Fig. 2c. Owing to the fabrication process, a proportion of the strands is shorter than the total PSF length, which results in a longitudinally variable cross-section. Accordingly, localized modes change adiabatically during propagation. Thus, the light beam expands throughout transport. A point input will expand until, on average, it reaches a width  $\sigma_{PSF} > l_{loc}$ . Thus, during light transport, we expect to lose resolution, as sketched in Fig. 2c.

**Quantum light transport.** The previous section introduced the central component of our experiment as shown in Fig. 1, the phase-separated fiber. Here, we outline the two other main experimental components, corresponding to the left and right sides of Fig. 1: generating quantum correlated states by means of SPDC, and the spatially resolved detection of these states with single-photon cameras. We conclude this section by demonstrating quantum light transport mediated by the localized modes in a PSF.

**Quantum anti-correlated light.** In order to show that quantum correlations of photons are maintained after propagating through

PSF, we prepared a source of non-classical light. Here, we pumped a periodically poled potassium titanyl phosphate (ppKTP) crystal with a CW laser at 405 nm wavelength in order to produce photon pairs at 810 nm by spontaneous parametric down-conversion (SPDC) (see Methods for details). By imaging the far-field of the SPDC emission plane, one obtains photon pairs that, by momentum conservation rules, are anti-correlated in space. Their joint distribution can be represented as follows<sup>23</sup>:

$$\Psi(\mathbf{r}_i, \mathbf{r}_j) = \frac{\sigma_+ \sigma_-}{\pi} \exp \left[ -\frac{\sigma_+^2}{4} |\mathbf{r}_i + \mathbf{r}_j|^2 - \frac{\sigma_-^2}{4} |\mathbf{r}_i - \mathbf{r}_j|^2 \right], \quad (1)$$

where  $\mathbf{r}_i$  and  $\mathbf{r}_j$  represent the transverse positions of the two photons, and  $\sigma_+^{-1}$  ( $\sigma_-$ ) is the width of the anti-correlation (correlation) in the crystal far-field (near-field) (details in Supplementary Information, Supplementary Note 3: Theory of SPDC quantum correlations). (Anti-)correlated photon pairs are the critical resource for quantum imaging protocols such as ghost imaging or imaging in the presence of high noise<sup>9</sup>. Therefore, showing that  $\sigma_+^{-1}$  remains small after propagating through the PSF would demonstrate the suitability of TALOF for quantum imaging.

**Imaging non-classical light with a single-photon camera.** We can experimentally estimate the anti-correlation width  $\sigma_+^{-1}$  by measuring spatially resolved photon coincidences (simultaneous detection of two photons), which are directly proportional to  $|\Psi|^2$ , the modulus-squared of Eq. (1) (see Supplementary Information, Supplementary Note 3: Theory of SPDC quantum correlations). Photon coincidences are straightforward to retrieve using single photon avalanche diode (SPAD) array cameras with detection timestamping capability<sup>24</sup>. Here, we use a recently developed high-speed SPAD array camera, which is optimized for quantum optics experiments with multi-photon coincidence events<sup>25</sup>. See Methods for further details of the SPAD array camera used. For a given acquisition with integration time  $T$ , our camera provides a list of detections with pixel coordinates and timestamps, at temporal resolution of  $\tau = 2$  ns. The spatially resolved coincidences between any pair of pixels are then calculated according to

$$cc_{i,j} = \sum_{l=1}^N I_{l,i} I_{l,j} - \frac{1}{N} \sum_{m,n=1}^N I_{m,i} I_{n,j}. \quad (2)$$

Here,  $N = T/\tau$  is the acquisition time expressed in timestamps, and  $I_{l,i} \in \{0, 1\}$  represents the value returned by the  $i^{\text{th}}$  pixel for the  $l^{\text{th}}$  timestamp, with  $I_{l,i} = 1$  if a detection was registered and  $I_{l,i} = 0$  if there is no registered detection. The right term accounts for removing accidentals. The spatial coordinates of the camera pixels correspond to the photons' positions in Eq. (1), i.e.,  $cc_{i,j} \equiv cc(\mathbf{r}_i, \mathbf{r}_j)$ . The anti-correlation parameter  $\sigma_+^{-1}$  can then be obtained directly by projecting the coincidences  $cc(\mathbf{r}_i, \mathbf{r}_j)$  into the sum coordinates  $\mathbf{r}_i + \mathbf{r}_j$ . This can be seen from Eq. (1), which shows that in the presence of SPDC anti-correlations, photon coincidences projected into the sum coordinates will show a peak at  $\mathbf{r}_i + \mathbf{r}_j = 0$ , with Gaussian width  $\sigma_+^{-126}$ .

One drawback of SPAD array cameras is that inter-pixel cross-talk leads to spurious coincidence detections<sup>27</sup>. We used a statistical method to remove these spurious coincidences, which was able to mitigate the effect of cross-talk. Details of cross-talk subtraction can be found in Supplementary Information, Supplementary Note 4: SPAD array cross-talk subtraction.

**Propagating quantum anti-correlations through fiber.** Figure 3a shows an intensity image of the SPDC emission, described by Eq. (1), to be coupled into the PSF; that is, before propagating through the fiber cane. Figure 3b, c show coincidences counts

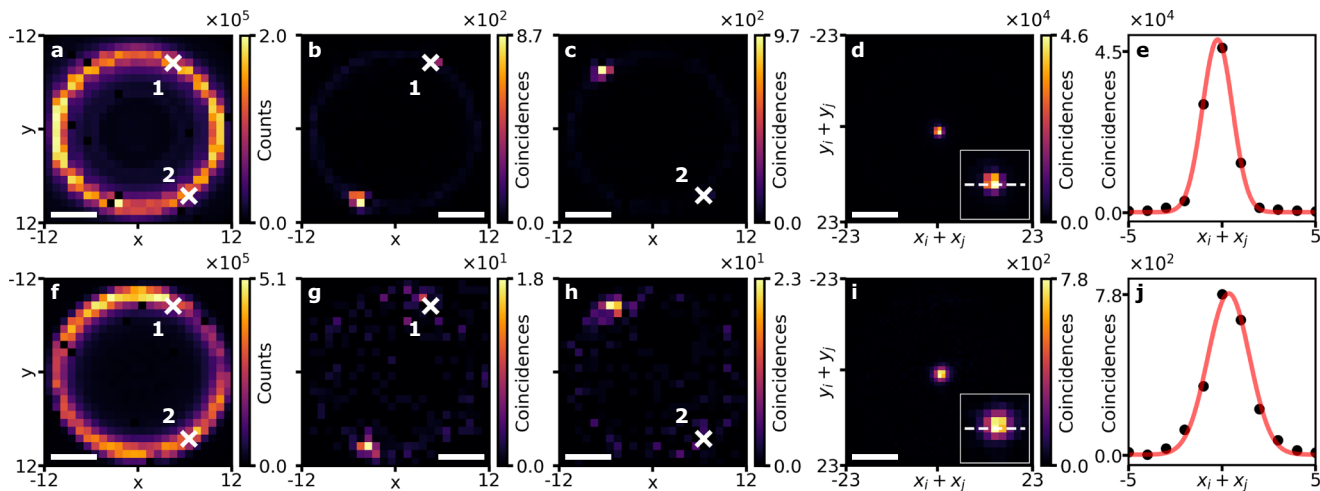


**Fig. 3** Wide-field propagation of quantum light through phase-separated fiber, imaged with a single-photon avalanche diode array camera. **a** Input intensity image. The color bar depicts the number of total single-photon counts per pixel, which accumulate over acquisition time. Scale bar, 400  $\mu\text{m}$ . **b, c** Input coincidences with single fixed pixel indicated by “X”, with pixel locations on spontaneous parametric down-conversion ring also shown in **a**. Color bars quantify coincidences per pixel. Scale bar, 400  $\mu\text{m}$ . **d** All input coincidences projected into sum-coordinates  $\mathbf{r}_i + \mathbf{r}_j$ . Inset shows close-up of peak. Color bar quantifies coincidences projected into the sum-coordinates. Scale bar, 800  $\mu\text{m}$ . **e** Cross-section along dashed white line in **d**, showing experimental values (black dots) and Gaussian fitting (solid red). **f–j** are analogous to **a–e**, respectively, and show coincidences after propagating through PSF.

with example pixels, illustrating how anti-correlated photon pairs are located at opposite sides of the ring-shaped emission profile. Figure 3d displays the coincidences detected before the PSF, mapped into the sum-coordinates space, exhibiting a strong peak around  $\mathbf{r}_i + \mathbf{r}_j = 0$ , which demonstrates the quantum nature of the SPDC light<sup>24,28</sup>.

By fitting a symmetric two-dimensional Gaussian to this peak, we estimate an input anti-correlation width of  $\sigma_+^{-1} \approx (52.7 \pm 0.3) \mu\text{m}$ . The inset of Fig. 3d shows a close-up of the central anti-correlation peak, while Fig. 3e shows a 1D profile and corresponding Gaussian fitting.

At the output of the TALOF, we expect that resolution has decreased due to the changing lateral cross-section, as sketched in Fig. 2c and discussed in the corresponding section. Figure 3f shows an intensity image of the SPDC photons after transport through the PSF where the ring shape of the profile is maintained compared to Fig. 3a. Figure 3g, h show coincidences for the same single example pixels as in Fig. 3b, c (indicated by “X”). Here, photon pairs are again clearly detected at opposite sides of the SPDC ring, showing that the SPDC anti-correlation was preserved. Figure 3i shows all the detected coincidences at the PSF output, mapped into the sum-coordinates as in Fig. 3d, showing again the prominent central peak due to SPDC anti-correlated photon pairs. The inset in Fig. 3i displays a close-up of the central peak, while Fig. 3j shows a cross-section of the sum-coordinate projected coincidences and the Gaussian fitting. After transport through the PSF, the fitted anti-correlation width was  $\sigma_+^{-1} = (73.3 \pm 0.5) \mu\text{m}$ .

Therefore, overall this result demonstrates that the quantum anti-correlation of the SPDC photon pairs are preserved after propagating through the PSF.

**Experimental characterization of wavelength dependence.** In the previous section, we observed that the anti-correlation width increased after propagating through the PSF, from  $\sigma_+^{-1} \approx (52.7 \pm 0.3) \mu\text{m}$  to  $\sigma_+^{-1} = (73.3 \pm 0.5) \mu\text{m}$ . Qualitatively, such an expansion can be expected based on Fig. 2c. A natural question is then whether the transport of quantum correlations through PSF can be improved: how can we minimize the blur of the correlation strength  $\sigma_+^{-1}$  during propagation? To answer this

question quantitatively, here we perform a scaling analysis of PSF. The purpose of this analysis is to provide insight on how to minimize the expansion of the anti-correlation width by optimizing PSF design and fabrication.

We conjecture that our PSF samples are not yet optimized; in particular, not for transport at the quantum light wavelength of 810 nm. In order to improve quantum light transport, in our subsequent analysis, we conduct experiments with classical light, which we complement with numerical simulations.

As discussed in the literature, for the design of a PSF-type TALOF (Abdullaev-Abdullaev mechanism), one has to choose a proper feature diameter  $d$  in order to achieve minimal  $h_{\text{loc}}$  for a given light wavelength  $\lambda$ <sup>29</sup>. In theory, the smallest  $h_{\text{loc}}$  should occur when the Ioffe-Regel condition<sup>30</sup> is fulfilled,  $k_T l^* \approx 1$ .

Here, the absolute value of the transverse wave vector  $k_T = \|\mathbf{k}_x + \mathbf{k}_y\|$  has to be about the inverse of the mean free path in the transverse plane,  $l^*$ . This criterion is however difficult to apply to TALOF design, as it does not directly state what the best diameter  $d$  is. As summarized from various theoretical studies by Mafi et al.<sup>29</sup>,  $d$  has an optimal value, which is on the order of magnitude of  $\lambda$ . Intuitively, for  $d \ll \lambda$ , the cross-section approaches an ordered effective medium, and  $l^*$  will become large. Contrarily, for  $d \gg \lambda$ , the light equally experiences low transverse disorder. Thus, when moving away from the condition  $d \sim \lambda$  in any direction, either by varying  $\lambda$  for a fixed  $d$  or vice versa,  $h_{\text{loc}}$ , and with it  $\sigma_{\text{PSF}}$ , increases.

In order to optimize transport, we conduct a scaling analysis, scanning over various values of  $\lambda/d$ . Owing to the scale invariance of Maxwell’s equations, adapting light wavelength or geometry is equivalent. Experimentally, it is much more straightforward to fix  $d$  by using the same PSF and to vary the wavelength of illumination. For this, we use classical light sources (lasers), as our degenerate photon pair source does not have tunable wavelength. We experimentally determined  $\sigma_{\text{PSF}}$ , while also performing actual imaging, for different wavelengths spanning over the visible spectrum. We then set the experimental results against numerical simulations.

We present the results from simulation and experiment in Fig. 4. With the previously discussed numerical simulations (more details in Methods) we calculated and compared localized modes for different light wavelengths. We based the simulations

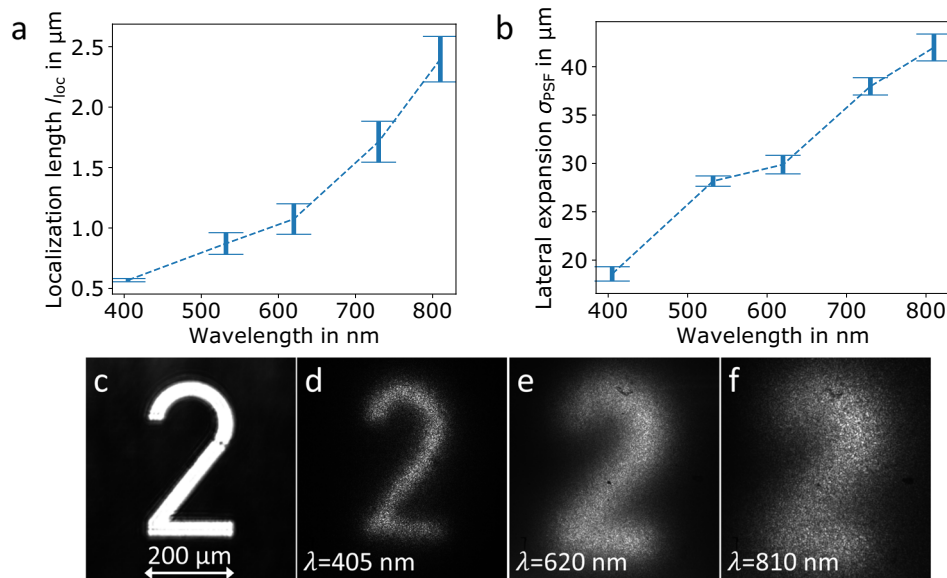


**Fig. 4 Scaling analysis: simulation and experiment.** Propagation parameters in phase-separated fiber (PSF) for different wavelengths. **a** Mean localization length (localized mode size,  $l_{\text{loc}}$ ), obtained from numerical simulation, based on a contrast image of the PSF cross-section (see Methods). The localization length increases with the wavelength. We calculated the error bars as the sample s.d. for the 5 smallest localized modes per data point (wavelength). **b** As a comparison, we display experimental data: the lateral expansion during transport through PSF, defined as s.d.  $\sigma_{\text{PSF}}$  of a Gaussian point-spread function. As the localized modes from **a** enlarge, so does  $\sigma_{\text{PSF}}$ . The error bars show the sample s.d. over 17–18 measurements per data point (wavelength  $\lambda$ ). **c–f** Wavelength-dependent image transport; the same input **c** transported through the same part of the PSF. Image quality degrades throughout the visible spectrum when increasing the wavelength of light.

on a contrast image as in Fig. 2a. We define the localization length by means of the inverse participation ratio  $P = \sum_i |l(i)| / \sum_i |l(i)|^2$ . We calculate  $P$  for several modes and average, yielding  $\langle P \rangle$ , where the uncertainty is the sample s.d. From that, we obtain  $l_{\text{loc}} = \langle P \rangle^{-1/2}$ . Fig. 4a shows the mean  $l_{\text{loc}}$  for a range of wavelengths, including the quantum light wavelength of 810 nm. For every data point, we averaged over the 5 found most tightly localized modes in the contrast image cross-section. The error bars show the sample s.d. over these 5 values (for every wavelength, respectively). It can be seen that the localization length increases faster than linearly from 405 to 810 nm.

Figure 4b provides the experimentally determined expansion during transport,  $\sigma_{\text{PSF}}$ , to be compared with the localization length from (a). Our definition of  $\sigma_{\text{PSF}}$  is as follows: we model the change of the input intensity pattern during transport as a convolution with a Gaussian point-spread function. The standard deviation parameter of this Gaussian is  $\sigma_{\text{PSF}}$  (see Fig. 2c and Supplementary Information, Supplementary Note 2: Lateral expansion during transport and effective numerical aperture). The error bars show the sample s.d. over 17–18 measurements per wavelength. It can be seen that the lateral expansion during transport (loss of resolution) is an order of magnitude higher than the fundamental resolution limit, the localization length from Fig. 4a. This is likely due to the finite mode density of the cross-section and non-perfect samples (changing cross-section). However, relatively, the increase of lateral expansion is significantly less pronounced. With the observed increasing  $\sigma_{\text{PSF}}$  for increasing wavelength, we correspondingly expect image transport quality to degrade.

In order to confirm this expectation, in Fig. 4c–f, we show an image formed with light of different wavelengths, propagated through PSF. We generated the image by illuminating the number “2” on a test target (see Methods), while scanning the probe wavelength  $\lambda$ . The quality of the propagated patterns degrades with increasing  $\lambda$  from 405 nm to 810 nm (from left to right in Fig. 4c–f).

The results confirm that the present PSF samples are not optimized for the quantum light wavelength. We also verify that the wavelength dependence is as expected from the PSF geometry, so that optimal (for this sample)  $\lambda \lesssim 405$  nm is on the order of magnitude of  $d \sim 280$  nm.

## Discussion

We have demonstrated that PSF can transmit photonic quantum correlations, as well as high-resolution classical images. Combined with its scalable fabrication process, we have therefore demonstrated a proof-of-principle of the essential ingredients for correlated quantum imaging and quantum communication applications. We emphasize the uniqueness of TALOF as a passive optical material that does not require precise alignment for efficient injection of quantum light into guiding optical modes, a notable advantage compared to multi-core fiber<sup>31</sup>. Additionally, TALOF can be resilient to bending<sup>11</sup>. In multi-mode fiber, on the other hand, active input control is required for maintaining correlations of quantum states after propagation<sup>10</sup>. Alternatively, when using free space optics, conjugates of the SPDC far-field/near-field planes must be controlled at every stage of the protocol<sup>23</sup>.

Our quantum light experiment (see Fig. 4b) shows that during transport resolution is reduced, that is, the PSF blurs the input. In particular, with the classical light experiment we find that for 810 nm wavelength this blurring is characterized by a Gaussian point spread function with width  $\sigma_{\text{PSF}} = (42.0 \pm 1.4)$   $\mu\text{m}$  (top right point in Fig. 4b). In the quantum light experiment, the input consists of 810 nm SPDC photon pairs with anti-correlation width  $\sigma_{+}^{-1} = (52.7 \pm 0.3)$   $\mu\text{m}$ . At the PSF output, due to the blurring incurred during transport, we therefore expect  $\sigma_{+}^{-1}$  to increase to  $(69.0 \pm 1.2)$   $\mu\text{m}$  (details in Methods). The experimentally detected transmitted quantum light had a fitted anti-correlation width of  $\sigma_{+}^{-1} = (73.3 \pm 0.5)$   $\mu\text{m}$ , which is comparable to the expected value of  $(69.0 \pm 1.2)$   $\mu\text{m}$ . The deviation between expected and measured value can be accounted for by the

experimental conditions for classical and quantum experiments not matching perfectly: we observed that point-spread function and attenuation vary over the PSF cross-section. To characterize  $\sigma_{\text{PSF}}$  (Fig. 4b), we scanned different positions over a line (see Supplementary Information, Supplementary Note 2: Lateral expansion during transport and effective numerical aperture, Supplementary Fig. S2). However, the SPDC ring represents a macroscopic input image covering a far larger area, which thus may have included cross-section positions with less favorable waveguiding properties than those described by  $\sigma_{\text{PSF}}$ . Overall, we have demonstrated here that the classical light experiments produce a valid description of the point-spread function also for quantum light transport.

We note that fabrication of TALOF so far has been predominantly based on the stack-and-draw method<sup>32</sup>, requiring pre-processing and mixing of tens of thousands of individual fibers. Apart from being highly laborious, this process is prone to introducing impurities. Laser writing so far yields low refractive index differences<sup>18</sup>. In contrast, we fabricate PSF in a novel more scalable procedure and from a single material. Notwithstanding this major advantage, fabrication process parameters (e.g., thermal cycle) are at present not yet optimized and need further improvement. In particular, two main issues prevent adoption of the current PSF generation in wide-scale quantum use cases: significant optical losses ( $\approx -4.8$  dB/cm at 810 nm), and less ideal light transport at near-infrared than for shorter-wavelength visible and ultraviolet light.

First, reducing optical losses requires eliminating what we believe to be the dominant source of attenuation: the longitudinal discontinuities in PSF. In fabrication, this implies initiating the phase separation process in a smaller volume, and maintaining it until the non-continuous glass phase has grown to larger particles than presently. This would enable more extreme elongation to strands, such that fewer discontinuities occur per fiber length. An additional reason for loss is the roughness of the PSF facets—this can be addressed by producing thinner samples, which can be cleaved.

Second, as can be seen in Fig. 4, we observed wavelength-dependent behavior in PS-TALOF. So far, the question if a wavelength dependence of localization in TALOF exists has not been settled in the literature<sup>33–37</sup>. Experimentally, when moving to the longer-wavelength portion of the visible spectrum we see higher blur during transport, and we confirm this qualitatively in actual image transport. We attribute the increasing degradation to less confined localized modes; our numerical simulations yield indeed an increase of localization length with increasing wavelength. In particular, at the 810 nm wavelength of the anti-correlated SPDC photon pairs, image transport is highly sub-optimal compared to short-wavelength visible light. As discussed above, currently at 810 nm the input anti-correlation width of  $\approx 52.7$   $\mu\text{m}$  is blurred to become  $\sim 30\%$  wider at output. With quantum light from the lower end of the visible spectrum, this spread would be significantly less, see Fig. 4b. For hypothetical 405 nm photon pairs with otherwise equal properties, the peak would broaden only minimally, from  $\approx 52.7$   $\mu\text{m}$  to  $\approx 52.8$   $\mu\text{m}$ . Thus, with the present samples significant improvement can be achieved by employing quantum light sources at shorter wavelengths<sup>38</sup>, a doubly promising approach due to the higher quantum efficiencies of SPAD array detectors at shorter wavelengths<sup>39</sup>. Equivalently, this line of reasoning indicates that the same improvement is possible not only by decreasing the quantum light wavelength; alternatively, fabrication can be adapted to produce other sample geometries (scale invariance of Maxwell's equations). We show that degradation occurs because the strands' diameters ( $d$ ) are small compared to the light wavelength. These results show that it is desirable to increase  $d$  in

PSF, such that the localized modes are more tightly confined (for visible and near-infrared light). Concretely, in our experiment, this would mean lower expansion of the sum coordinate peak during propagation through PSF (Fig. 3d, i). Transport of near-infrared light is potentially relevant for quantum imaging (e.g., of biological tissue) as well as quantum communications (telecom).

In conclusion, we have demonstrated a platform for quantum-enabled applications on the basis of transverse Anderson localization, where the scalable fabrication procedure of the PSF makes it attractive for real-world devices. We identified current limitations of our system and made technologically feasible suggestions for future optimization. The present work thus represents only the tip of the iceberg of studies with TALOFs transporting quantum light, with further advances likely to enable a large range of use cases in quantum imaging and communication applications such as high-resolution endoscopy, entanglement distribution and quantum key distribution.

## Methods

**Sample post-processing and material analysis.** We performed all analyses shown in this work with PSFs of external diameter 1.6 mm. For imaging, the cane length was 36 mm. The inclusions had higher refractive index; Table 1 specifies the exact glass composition.

For a theoretical treatment on the elongation of phase-separated glass we refer to a work by Seward<sup>19</sup>. Both cane facets were machine-polished (Logitech PM5), using an emulsion containing DI water and 30 to 40 nm alumina particles. This polishing decreases the roughness of the surface to improve image transport. However, the glass phases have different hardness; this is why we could image the structure of PSF by taking a topology AFM image. There, the strands were found to be around 10 nm deeper than the matrix glass. Subsequently, with the software ImageJ<sup>40</sup> we identified particles (excluding particles on the edges) in order to obtain statistics of the strand sizes. The resulting distribution is displayed in Fig. 5. Here, by assuming that the strands have circular cross-section we converted strand areas to strand diameters  $d_i$ , which are shown on the  $x$ -axis (equidistant bins). On the  $y$ -axis, the total area covered by all strands of this  $d_i$  can be found. The distribution resembles a Poissonian shape with mean strand diameter of roughly  $d \approx 280$  nm.

From the same data, we calculate the filling fraction of the elongated strands phase (relative area with respect to the total area of the cross-section) to 26%.

The refractive index of bulk samples of the two pure glass phases was measured with a refractometer (Bausch and Lomb Low Range Precision) for a wide range of optical wavelengths. After a fit to a three-term Sellmeier equation, for 810 nm light the refractive indices are 1.60 (strands) and 1.47 (matrix), yielding a refractive index contrast of 0.13.

**Quantum light experiment.** As shown in Fig. 6 we generate SPDC photon pairs using a CW single-mode laser (Toptica TOPMODE 405) at 405 nm as pump. We focus the pump with a lens  $F_1 = 300$  mm into a ppKTP crystal (Raicol,

**Table 1 Phase-separated glass composition in weight %.**

SiO <sub>2</sub>	B <sub>2</sub> O <sub>3</sub>	Al <sub>2</sub> O <sub>3</sub>	Na <sub>2</sub> O	P <sub>2</sub> O <sub>5</sub>	CaO	BaO
70.5	13	1.5	3	1	5	6

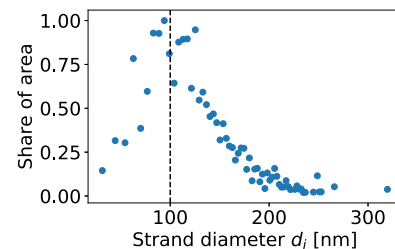


**Fig. 5 Feature statistics of a phase-separated fiber contrast image.** Strand diameter statistics based on the cross-section contrast image from Fig. 2a. The distribution of equidistantly binned strand diameters  $d_i$  ( $x$ -axis) is plotted against the total area (on the  $y$ -axis) covered by all similarly large strands. The dashed line roughly indicates the average strand diameter  $d$ .

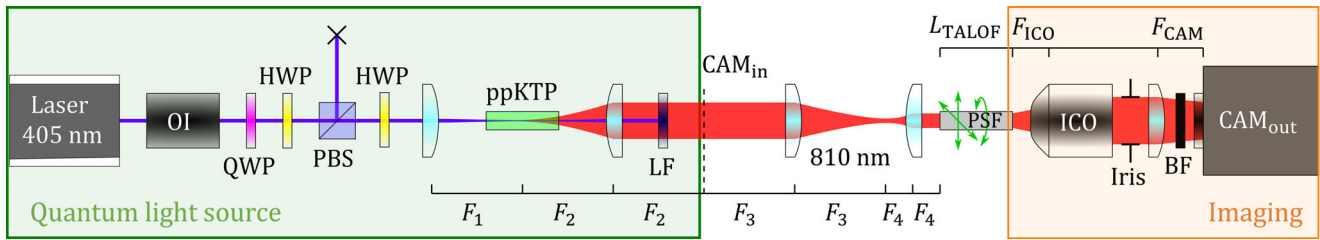


**Fig. 6 Setup for quantum correlations transport experiment.** We generated correlated photon pairs in our quantum light source: a linearly polarized 405 nm laser beam passes through an optical isolator; the laser power is controlled by beams of a polarizing beam splitter. The laser pumps a periodically poled KTP crystal, where correlated photon pairs are generated via SPDC. We measured the photon pairs before (dashed line,  $CAM_{in}$ ) and after propagating through the phase-separated fiber (PSF) ( $CAM_{out}$ ).  $L_{TALOF}$  denotes the length of the PSF. We imaged the far-field of photon pair generation in the crystal onto the PSF input facet and captured the PSF output facet with the SPAD array camera. A bandpass filter before camera sensor rejects stray light. QWP quarter-wave plate, HWP half-wave plate, PBS polarizing beam splitter, OI optical isolator, LF long-pass filter (LF), ICO infinity corrected objective, BF bandpass filter. Focal lengths  $F_{ICO}$ ,  $F_{CAM}$ ,  $F_1$ ,  $F_2$ ,  $F_3$ ,  $F_4$  are discussed in the corresponding text.

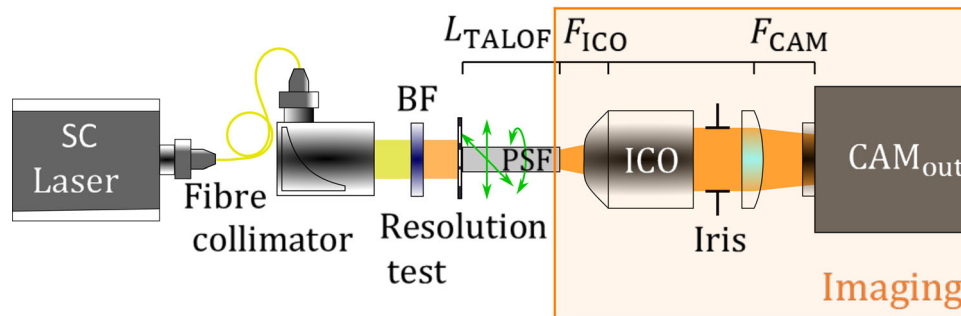


**Fig. 7 Setup for classical light experiments.** Classical imaging apparatus. White light from the supercontinuum (SC) laser is collimated and filtered with a bandpass filter (BF). Images are generated with a resolution test target and inserted into the PSF directly without any optics; that is, resolution test target and phase-separated fiber (PSF) are in contact.  $L_{TALOF}$  denotes the length of the PSF. An infinity-corrected objective (ICO) collects the PSF output. A CMOS camera ( $CAM_{out}$ ) captures images. Focal lengths  $F_{ICO}$ ,  $F_{CAM}$  are discussed in the corresponding text.

$2 \times 1 \times 20$  mm) to generate type-0 SPDC non-classical photon pairs centered at 810 nm. The ppKTP crystal is maintained at 141 °C by a resistive oven (Covesion) in order to satisfy the degenerate phase-matching condition, and produces an SPDC output ring with diameter  $D_{SPDC} \approx 1.1$  mm (measured at  $CAM_{in}$ , with an additional de-magnification of 1:4 in Fig. 6). A lens  $F_2 = 100$  mm images the SPDC emission onto the far-field of the ppKTP crystal plane, producing spatially anti-correlated photon pairs (see Supplementary Information, Supplementary Note 3: Theory of SPDC quantum correlations). Two additional lenses with  $F_3 = 300$  mm and  $F_4 = 100$  mm image the anti-correlated photon pairs onto the PSF entrance facet with a magnification  $M = 1/3$ . The PSF output facet is imaged (at  $CAM_{out}$  in Fig. 6) using an infinity corrected objective (ICO, Edmund Optics), which has nominal 2x magnification when used with a 200 mm tube lens. Here, we use a lens with  $F_{CAM} = 75$  mm to image the light onto the camera sensor, yielding a magnification of 0.75 from the PSF facet to the camera. PSF input and output imaging system magnifications are taken into account when calculating the SPDC photon pairs' intensity profile and anti-correlation widths in the reference frame of the PSF. Intensity images and coincidence counts of the SPDC photon pairs were measured using a recently developed SPAD array camera that is optimized for photon coincidence detection in the sparse illumination regime<sup>25</sup>. This SPAD camera has  $24 \times 24$  pixels with  $50 \mu\text{m}$  pixel pitch, and uses a microlens array to achieve a fill factor of around 60%. This is considering non-ideal placement of the microlens array and non-perfect alignment of the light beam. Taking into account the fill factor, the photon detection efficiency at 810 nm is  $\sim 9\%$ . Before the PSF we measured a coincidence rate (after post-processing, i.e., removal of accidentals and cross-talk) of  $4.78 \times 10^5$  photon pairs per second over a 1.08 s acquisition time, whereas after the PSF we measured a rate of  $1.32 \times 10^2$  coincidences per second over a 101.32 s acquisition time, which gives us an effective optical loss of  $\approx -4.81$  dB/cm at 810 nm.

**Broadening of anti-correlation peak after propagation.** To calculate the expected broadening of the input SPDC anti-correlation peak (Fig. 3d) in accordance with the PSF wave-guiding properties (Fig. 4b), we numerically blur the pre-transport coincidence data. In particular, the  $24 \times 24$  two-dimensional array  $cc(\mathbf{r}|\mathbf{r}_i)$  corresponds to the photon counts conditional on detection at  $\mathbf{r}_i$ , that is, the map of all coincidences with the single fixed pixel  $\mathbf{r}_i$  (where  $\mathbf{r} \equiv [x, y]$ ). For every  $i^{\text{th}}$  pixel, we therefore convolute the input coincidences  $cc^{in}(\mathbf{r}|\mathbf{r}_i)$  with a Gaussian function,

with width  $\sigma_{PSF} = (42.0 \pm 1.4) \mu\text{m}$  (see Fig. 4b), to obtain the expected blurred output:

$$cc^{blur}(\mathbf{r}|\mathbf{r}_i) = A \exp(-r^2/2\sigma_{PSF}^2) * cc^{in}(\mathbf{r}|\mathbf{r}_i), \quad (3)$$

where  $*$  denotes convolution and  $A$  is a normalization parameter. The numerically blurred coincidences are projected into sum coordinates, and again we fit a symmetric 2D Gaussian, obtaining the expected output anti-correlation width  $\sigma_{+}^{-1} = (69.0 \pm 1.2) \mu\text{m}$ .

**Mode simulation.** The simulation was computed for a contrast image with edge length of about  $10 \mu\text{m}$  of a representative part of the PSF cross-section; one finite element corresponded to one pixel of the  $512 \times 512$  image.

The software package we used, MIT Photonic Bands<sup>32</sup>, employs periodic boundary conditions to calculate modes in frequency space; it solves the wave equation

$$i \frac{\partial A}{\partial z} + \frac{1}{2k} \nabla_{\perp}^2 A + \frac{k}{n_0} \Delta n(x, y) A = 0, \quad (4)$$

where we extract  $n(x, y)$  from the contrast image. When the simulated area is large compared with the localized modes, we see no effects of the boundary conditions. We note that other types of simulations starting from scanning probe microscopy images of TALOF can be found in the literature<sup>41</sup>.

**Setup for classical light experiments.** The PSF sample was mounted on a motorized 6-axis stage as shown in Fig. 7. Here, a collimated beam with diameter  $D_s = 4$  mm (at  $1/e^2$ ) from a supercontinuum laser (NKT Photonics SuperK, denoted SC Laser) was used as light source. Its IR spectrum was removed by using a shortpass filter (SF), while specific visible regions were selected with additional bandpass filters (BFs) with FWHM = 10 nm (Thorlabs), centered at 532, 620, 730, and 810 nm. For 405 nm, we employed a diode laser (Toptica TOPMODE-405).

We measured the optical properties of PSF canes with the setup shown in Fig. 7. First, we studied the resolution of our sample through the point spread function, defined as the Gaussian spreading of a circular input beam, by injecting light through a pinhole aperture (RT) of diameter  $D_{RT} = 40 \mu\text{m}$ , mounted at the fiber entrance. We imaged the near-field of the output facet by using a 20x infinity

corrected objective (ICO) with focal length  $F_{\text{ICO}} = 10$  mm followed by a tube lens of  $F_{\text{CAM}} = 200$  mm, then using a magnification  $M = 20\times$ . Secondly, we replaced the aperture by a negative 1951-USAF test target resolution test (Edmund Optics #55-622). Here, we compared propagated patterns at different wavelengths as shown in Fig. 4c–e for analyzing their similarity as described below. A CMOS camera (model IDS UI-3882LE-M-VU) with  $3088 \times 2076$  pixels of  $2.4 \mu\text{m}$  pitch was used as imaging device.

### Data availability

All data needed for the conclusions are in the manuscript and supplementary information. The datasets generated during and/or analyzed during the current study are available from the corresponding author on reasonable request.

Received: 1 February 2022; Accepted: 7 October 2022;

Published online: 26 October 2022

### References

- Anderson, P. W. Absence of diffusion in certain random lattices. *Phys. Rev.* **109**, 1492–1505 (1958).
- Abdullaev, S. S. & Abdullaev, F. K. On propagation of light in fiber bundles with random parameters. *Radiophys. Quant. Electron.* **23**, 766 (1980).
- De Raedt, H., Lagendijk, A. D. & de Vries, P. Transverse localization of light. *Phys. Rev. Lett.* **62**, <https://doi.org/10.1103/PhysRevLett.62.47> (1989).
- Schwartz, T., Bartal, G., Fishman, S. & Segev, M. Transport and Anderson localization in disordered two-dimensional photonic lattices. *Nature* **446**, 52–55 (2007).
- Mafi, A., Ballato, J., Koch, K. W. & Schülzgen, A. Disordered Anderson localization optical fibers for image transport—A review. *J. Lightwave Technol.* **37**, 5652–5659 (2019).
- Karbasi, S. et al. Image transport through a disordered optical fibre mediated by transverse Anderson localization. *Nat. Commun.* **5**, 3362 (2014).
- Ding, Y. et al. High-dimensional quantum key distribution based on multicore fiber using silicon photonic integrated circuits. *npj Quantum Inf.* **3**, 1–7 (2017).
- Gregory, T., Moreau, P.-A., Toninelli, E. & Padgett, M. J. Imaging through noise with quantum illumination. *Sci. Adv.* **6**, eaay2652 (2020).
- Moreau, P.-A., Toninelli, E., Gregory, T. & Padgett, M. J. Imaging with quantum states of light. *Nat. Rev. Phys.* **1**, 367–380 (2019).
- Defienne, H., Barbieri, M., Walmsley, I. A., Smith, B. J. & Gigan, S. Two-photon quantum walk in a multimode fiber. *Sci. Adv.* **2**, e1501054 (2016).
- Zhao, J. et al. Image transport through meter-long randomly disordered silica-air optical fiber. *Sci. Rep.* **8**, 3065 (2018).
- Karbasi, S. et al. Observation of transverse Anderson localization in an optical fiber. *Opt. Lett.* **37**, 2304 (2012).
- Tuan, T. H., Kuroyanagi, S., Nagasaka, K., Suzuki, T. & Ohishi, Y. Near-infrared optical image transport through an all-solid tellurite optical glass rod with transversely-disordered refractive index profile. *Opt. Express* **26**, 16054–16062 (2018).
- Tuggle, M. et al. Observation of optical nonlinearities in an all-solid transverse anderson localizing optical fiber. *Opt. Lett.* **45**, 599–602 (2020).
- Nakatani, A. et al. Transverse Anderson localization of mid-infrared light in a chalcogenide transversely disordered optical fiber. *Opt. Express* **30**, 5159–5166 (2022).
- Karbasi, S., Hawkins, T., Ballato, J., Koch, K. W. & Mafi, A. Transverse Anderson localization in a disordered glass optical fiber. *Optical Mater. Express* **2**, 1496 (2012).
- Chen, M. & Li, M.-J. In *Photonic and Phononic Properties of Engineered Nanostructures IV*, Vol. 8994, 176–182 (SPIE, 2014).
- Gianfrate, A., Dominici, L., Ballarini, D., Sanvitto, D. & Leonetti, M. Transverse localization of light in laser written designed disorder. *Appl. Phys. Lett.* **116**, 071101 (2020).
- Seward III, T. P. Elongation and spheroidization of phase-separated particles in glass. *J. Non-Crystalline Solids* **15**, 487–504 (1974).
- Randall, L. J. & Seward III, T. P. Pseudo-fiber optic devices. US Patent 3,870,399 (1975).
- Seward III, T. P. In *The Physics of Non-Crystalline Solids*. 342–347 (Trans Tech Publications, 1977).
- Johnson, S. G. & Joannopoulos, J. D. Block-iterative frequency-domain methods for maxwell's equations in a planewave basis. *Opt. Express* **8**, 173–190 (2001).
- Tasca, D. S., Walborn, S. P., Souto Ribeiro, P. H., Toscano, F. & Pellat-Finet, P. Propagation of transverse intensity correlations of a two-photon state. *Phys. Rev. A* **79**, 033801 (2009).
- Eckmann, B. et al. Characterization of space-momentum entangled photons with a time resolving CMOS SPAD array. *Opt. Express* **28**, 31553–31571 (2020).
- Madonini, F., Severini, F., Incoronato, A., Conca, E. & Villa, F. in *Quantum Optics and Photon Counting 2021*, Vol. 11771, 117710B (International Society for Optics and Photonics, 2021).
- Edgar, M. P. et al. Imaging high-dimensional spatial entanglement with a camera. *Nat. Commun.* **3**, 1–6 (2012).
- Rech, I. et al. Optical crosstalk in single photon avalanche diode arrays: a new complete model. *Opt. Express* **16**, 8381–8394 (2008).
- Ndagano, B. et al. Imaging and certifying high-dimensional entanglement with a single-photon avalanche diode camera. *npj Quantum Inf.* **6**, 1–8 (2020).
- Mafi, A. Transverse Anderson localization of light: a tutorial. *Adv. Opt. Photonics* **7**, 459 (2015).
- Ioffe, A. & Regel, A. In *Progress in Semiconductors Vol. 4: Non-crystalline Amorphous, and Liquid Electronic Semiconductors* (Heywood, 1960).
- Ortega, E. A. et al. Experimental space-division multiplexed polarization-entanglement distribution through 12 paths of a multicore fiber. *PRX Quantum* **2**, 040356 (2021).
- Mafi, A., Tuggle, M., Bassett, C., Mobini, E. & Ballato, J. Advances in the fabrication of disordered transverse Anderson localizing optical fibers [Invited]. *Optical Mater. Express* **9**, 2769 (2019).
- Karbasi, S., Koch, K. & Mafi, A. In *Frontiers in Optics, FTh1D-8* (Optical Society of America, 2012).
- Karbasi, S. et al. Detailed investigation of the impact of the fiber design parameters on the transverse Anderson localization of light in disordered optical fibers. *Opt. Express* **20**, 18692 (2012).
- Schirmacher, W., Abaie, B., Mafi, A., Ruocco, G. & Leonetti, M. What is the right theory for anderson localization of light? an experimental test. *Phys. Rev. Lett.* **120**, 067401 (2018).
- Roth, P. et al. Wavelength dependence of transverse Anderson localization in disordered glass-air fiber. In: *Proceedings of SPIE*, 3 (Charleston, South Carolina, United States, 2019).
- Giordani, T., Schirmacher, W., Ruocco, G. & Leonetti, M. Transverse and quantum localization of light: a review on theory and experiments. *Front. Phys.* **9** <https://doi.org/10.3389/fphy.2021.715663> (2021).
- Perna, A. S., Gräfe, M. & Steinlechner, F. In *CLEO: Applications and Technology, JTh3A-16* (Optical Society of America, 2021).
- Madonini, F., Severini, F., Zappa, F. & Villa, F. Single photon avalanche diode arrays for quantum imaging and microscopy. *Adv. Quantum Technol.* **4**, 2100005 (2021).
- Abràmoff, M. D., Magalhães, P. J. & Ram, S. J. Image processing with ImageJ. *Biophoton. Int.* **11**, 36–42 (2004).
- Abaie, B. & Mafi, A. Modal area statistics for transverse Anderson localization in disordered optical fibers. *Opt. Lett.* **43**, 3834 (2018).

### Acknowledgements

The authors would like to thank V. Finazzi for technical support and valuable discussions. This work has received funding from the European Union's Horizon 2020 FET-Open research and innovation program under grant agreement No. 801060 (Q-MIC), the Spanish State Research Agency through the CEX2019-000910-S [MCIN/ AEI/10.13039/501100011033]. This study was supported by MCIN with funding from European Union NextGenerationEU (PRTR-C17.I1) and by Generalitat de Catalunya; also by Fundació Cellex, Fundació Mir-Puig, and Generalitat de Catalunya through CERCA. A.D. acknowledges support of the ICFO CELLEX Ph.D.-fellowship. This project has received funding from the European Union's Horizon 2020 research and innovation program under the Marie Skłodowska-Curie grant agreement No. 713729. A.C.'s work was partially supported by Becas Chile No. 74200052 from ANID, Chile; also by CEX2019-000910-S [MCIN/ AEI/10.13039/501100011033], Fundació Cellex, Fundació Mir-Puig, and Generalitat de Catalunya through CERCA.

### Author contributions

V.P. and N.F.B. conceived the joint project; N.F.B., T.P.S., L.L., and K.W.K. designed and provided the disordered fiber canes. A.R., F.M., and F.V. developed the SPAD array camera. A.D. conducted the simulations; A.D., A.C., and R.C. performed the experiments, analyzed the data and wrote the manuscript with contributions from all authors. V.P. supervised the work.

### Competing interests

A.D., R.C., A.C., N.F.B., T.P.S., L.S., and V.P. are co-inventors of a patent application related to the results of this paper. All other authors declare no competing interests.



**Additional information**

**Supplementary information** The online version contains supplementary material available at <https://doi.org/10.1038/s42005-022-01036-5>.

**Correspondence** and requests for materials should be addressed to Alexander Demuth, Álvaro Cuevas or Valerio Pruneri.

**Peer review information** *Communications Physics* thanks Da-Wei Wang, Vladislav Yakovlev and the other, anonymous, reviewer(s) for their contribution to the peer review of this work.

**Reprints and permission information** is available at <http://www.nature.com/reprints>

**Publisher's note** Springer Nature remains neutral with regard to jurisdictional claims in published maps and institutional affiliations.



**Open Access** This article is licensed under a Creative Commons Attribution 4.0 International License, which permits use, sharing, adaptation, distribution and reproduction in any medium or format, as long as you give appropriate credit to the original author(s) and the source, provide a link to the Creative Commons license, and indicate if changes were made. The images or other third party material in this article are included in the article's Creative Commons license, unless indicated otherwise in a credit line to the material. If material is not included in the article's Creative Commons license and your intended use is not permitted by statutory regulation or exceeds the permitted use, you will need to obtain permission directly from the copyright holder. To view a copy of this license, visit <http://creativecommons.org/licenses/by/4.0/>.

© The Author(s) 2022